

Frequency-Weighted Robust Tensor Principal Component Analysis

Shenghan Wang, Yipeng Liu, *Senior Member, IEEE*, Lanlan Feng, Ce Zhu, *Fellow, IEEE*

Abstract

Robust tensor principal component analysis (RTPCA) can separate the low-rank component and sparse component from multidimensional data, which has been used successfully in several image applications. Its performance varies with different kinds of tensor decompositions, and the tensor singular value decomposition (t-SVD) is a popularly selected one. The standard t-SVD takes the discrete Fourier transform to exploit the residual in the 3rd mode in the decomposition. When minimizing the tensor nuclear norm related to t-SVD, all the frontal slices in frequency domain are optimized equally. In this paper, we incorporate frequency component analysis into t-SVD to enhance the RTPCA performance. Specially, different frequency bands are unequally weighted with respect to the corresponding physical meanings, and the frequency-weighted tensor nuclear norm can be obtained. Accordingly we rigorously deduce the frequency-weighted tensor singular value threshold operator, and apply it for low rank approximation subproblem in RTPCA. The newly obtained frequency-weighted RTPCA can be solved by alternating direction method of multipliers, and it is the first time that frequency analysis is taken in tensor principal component analysis. Numerical experiments on synthetic 3D data, color image denoising and background modeling verify that the proposed method outperforms the state-of-the-art algorithms both in accuracy and computational complexity.

Index Terms

tensor principal component analysis, tensor singular value decomposition, tensor nuclear norm, frequency component analysis, background extraction.

I. INTRODUCTION

Principal component analysis (PCA) [1] is a classical dimension reduction technique that performs low-rank component extraction for a matrix. One of its main problems is the sensitivity to outliers. A number of improved PCA methods have been proposed to deal with it [2]–[6]. Among them, robust principal component analysis (RPCA) is the first polynomial-time algorithm with strong performance guarantees [7], which has many successful applications including face recognition [8]–[10], background model initialization [11]–[13] and image recovery [14], [15]. RPCA is designed for two-way data, but dimension reduction is required for many multi-way data, such as color images, color video sequences and hyperspectral images. The matrix computation based RPCA requires to reshape these multi-way data into matrices, which would lead to data structure information loss [7], [16].

Tensor is higher order generalization of vector and matrix [17], [18], and it is a natural representation for multi-way data. In order to fully exploit the multidimensional structure of tensors, robust tensor principal component analysis (RTPCA) has been proposed by separating low-rank tensor component and sparse component of multi-way data [19]–[21]. Fig. 1 illustrates the model of RTPCA.

RTPCA methods vary with different tensor ranks. The canonical polyadic (CP) decomposition factorizes a tensor into the sum of several rank-one tensors [22]–[24]. The CP rank of a tensor is defined as the smallest number of rank-one tensors. Methods based on CP decomposition often assume that the CP rank of the target tensor is known [25], [26]. However, the CP rank of a tensor is NP-hard to compute [27]. Some works [28], [29] try to estimate the CP rank in Bayesian framework, but they often suffer from over-estimating or under-estimating the true CP rank. The Tucker decomposition decomposes a tensor into a core tensor multiplied by factor matrix along each mode [30], [31]. The Tucker rank is defined as the vector whose entries are the ranks of the factor matrices. As the nuclear norm is the convex envelope of the matrix rank, the sum of nuclear norms (SNN) has been proposed in the Tucker rank minimization problem [32]–[34]. In [21], [34], the authors successfully recover the low-rank and the sparse component from corrupted tensor based on SNN minimization. However, the Tucker decomposition has to unfold the tensors into matrices which needs high computation costs.

This research is supported by National Natural Science Foundation of China (NSFC, No. 61602091), Sichuan Science and Technology Program (No. 2019YFH0008, No. 2018JY0035). The corresponding author is Yipeng Liu.

All the authors are with School of Information and Communication Engineering, University of Electronic Science and Technology of China (UESTC), Chengdu, 611731, China, email: yipengliu@uestc.edu.cn

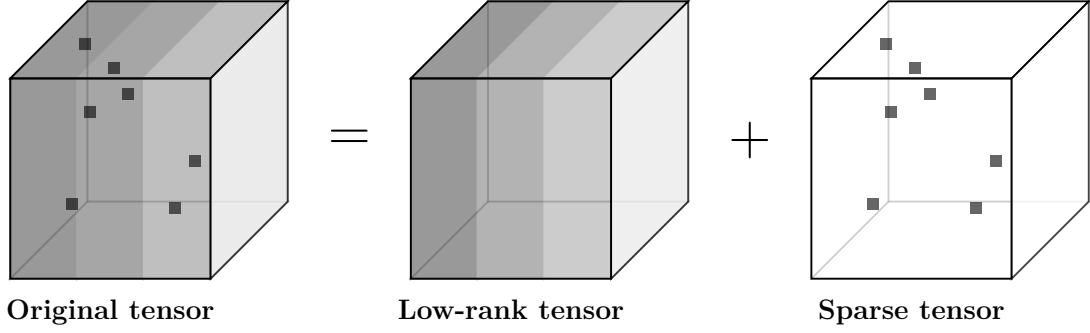


Fig. 1: Illustration of RTPCA method

Recently the tensor singular value decomposition (t-SVD) has been proposed [35]–[37], which factorizes a order-3 tensor as the tensor products of three tensors, as it shows in Fig. 4. The tubal rank, which is defined in t-SVD framework, can characterise the low-rank structure of a tensor very well [38]. The tubal rank minimization problem is usually relaxed into the tensor nuclear norm (TNN) minimization problem, which can be solved by convex optimization. There are different forms of TNN in the t-SVD based RTPCA [39]–[43], and several sparse constraints are used according to different applications [38], [44], [45]. Though t-SVD can be calculated easily in the Fourier domain, none of these works exploit the prior knowledge about frequency spectrum even when it is available in some applications.

Since larger singular values of a matrix indicate its underlying principal directions, it is unfair to shrink all the singular values with a same threshold when solving the nuclear norm minimization problem. Therefore, weighted nuclear norm (WNN) is proposed to adaptively assign weights on different singular values [14]. This data-driven strategy selects weights in each iteration according to the size of singular values in last iteration.

Motivated by the success of the WNN, we assign different weights on different frequency components in t-SVD for RTPCA. Thanks to the inherent property of t-SVD on frequency analysis, a new frequency-weighted tensor nuclear norm (FTNN) is formulated by incorporating Fourier filtering in t-SVD. To our best of knowledge, this is the first work to investigate the weighted tensor nuclear norm via Fourier analysis in the t-SVD framework. The main contributions are summarized as follows:

- 1) Combining the discrete Fourier transform (DFT) with t-SVD, we define a frequency-weighted tensor nuclear norm (FTNN) for t-SVD based rank minimization problem, which can better utilize the prior knowledge about frequency spectrum in t-SVD. The classical TNN can be regarded as a special case of FTNN. The corresponding frequency-weighted tensor singular value threshold (FTSVT) operator is rigorously deduced, which is crucial for solving low-rank approximation problems.
- 2) Equipped with the FTNN, a new optimization model called FTNN-RTPCA can be obtained for extraction of low-rank and sparse components. The alternating direction method of multipliers (ADMM) is used to divide the optimization model into low-rank approximation problem and sparse approximation problem. The former can be solved by the deduced FTSVT operator, while the well-known soft thresholding operator is for the latter.
- 3) Based on the frequency component analysis of visual data including color image and gray video, we find that these visual data accord with the proposed FTNN model. Numerical experiment on Synthetic 3D data verifies that FTNN based methods outperforms classical TNN based methods. Color image denoising experiment also shows the superior performance of FTNN-RTPCA compared with existing methods.
- 4) By analysing the nuclear norm distribution and frequency components, we discuss how to design the weighting vector. Besides, we design a special weighting vector and develop a SVD-free algorithm to deal with the background modeling problem. Experiments have shown that the proposed FTNN-RTPCA can effectively extract the background much faster than some state-of-the-art methods.

The rest of this paper is organized as follows. Section II gives some notations and preliminaries used in this paper. In Section III, we define a new FTNN, and propose the FTNN-RTPCA method. In Section IV, we first

discuss the setting of the weighting vector and verify it in synthetic experiments. Then we conduct some numerical experiments to compare the proposed method with some state-of-the-art algorithms including color image denoising and background model initialization. Section V gives a conclusion of this paper.

II. PRELIMINARIES AND RELATED WORKS

A. Notation

A scalar, a vector, a matrix and a tensor are denoted as a , \mathbf{a} , \mathbf{A} , \mathcal{A} . $\mathcal{A}^{(i_3)}$ denotes the i_3 -th frontal slice of \mathcal{A} . The tube fiber on the third mode is denoted as $\mathcal{A}(i_1, i_2, :)$.

The ℓ_1 norm and the Frobenius norm of a tensor are defined as $\|\mathcal{A}\|_1 = \sum_{i_1, i_2, i_3} |\mathcal{A}_{i_1, i_2, i_3}|$ and $\|\mathcal{A}\|_F = \sum_{i_1, i_2, i_3} |\mathcal{A}_{i_1, i_2, i_3}|^2$, respectively. When $I_3 = 1$, these tensor norms degenerate into corresponding matrix norms. The nuclear norm of a matrix is $\|\mathbf{A}\|_* = \sum_{i_0} \sigma_{i_0}(\mathbf{A})$, where $\sigma_{i_0}(\mathbf{A})$ with $I_0 = \min\{I_1, I_2\}$, is the i_0 -th singular values.

For a matrix \mathbf{A} , \mathbf{A}^H takes the complex conjugate transpose of all its entries, and \mathbf{A}^T is the transpose matrix. $\text{conj}(\mathbf{A})$ takes the complex conjugate matrix of \mathbf{A} . The sets of real and complex numbers are \mathbb{R} and \mathbb{C} , respectively. $\lceil x \rceil$ is the nearest integer which is equal or greater than x .

B. Discrete Fourier Transformation

As the discrete Fourier transformation (DFT) plays a vital role in the t-SVD, we provide a brief introduction of the notations and definitions about it. The frequency bands and frequency components of a order-3 tensor are defined in this subsection.

The discrete Fourier transformation (DFT) matrix is defined as:

$$\mathbf{F}_N = \begin{bmatrix} 1 & 1 & 1 & \cdots & 1 \\ 1 & \omega & \omega^2 & \cdots & \omega^{N-1} \\ \vdots & \vdots & \vdots & \ddots & \vdots \\ 1 & \omega^{N-1} & \omega^{2(N-1)} & \cdots & \omega^{(N-1)(N-1)} \end{bmatrix} \in \mathbb{C}^{N \times N}$$

where $\omega = \exp(-\frac{2\pi j}{N})$, where $j = \sqrt{-1}$. We can find that:

$$\mathbf{F}_N \mathbf{F}_N^H = \mathbf{F}_N^H \mathbf{F}_N = N\mathbf{I}, \quad \mathbf{F}_N^{-1} = \frac{1}{N} \mathbf{F}_N^H \quad (1)$$

The DFT for a vector $\mathbf{v} = [v_1, v_2, \dots, v_N]^T$ is denoted as $\bar{\mathbf{v}} = \mathbf{F}_N \mathbf{v} \in \mathbb{C}^N$, and the inverse DFT is represented as $\mathbf{v} = \mathbf{F}_N^{-1} \bar{\mathbf{v}} \in \mathbb{R}^N$. These two transforms can be efficiently calculated by fast Fourier transformation (FFT) and inverse fast Fourier transformation (IFFT).

As it can be deduced from the definition of DFT, we have one property as follows [46]:

$$\bar{v}_1 \in \mathbb{R}; \quad \text{conj}(\bar{v}_i) = \bar{v}_{N-n+2}, n = 2, 3, \dots, \left\lceil \frac{N+1}{2} \right\rceil \quad (2)$$

where $\bar{\mathbf{v}} = [\bar{v}_1, \bar{v}_2, \dots, \bar{v}_N]^T$.

To further analyze the spectral properties of this vector, we give the definitions of frequency band and frequency component.

Definition 1 (frequency band). For a vector $\mathbf{v} = [v_1, v_2, \dots, v_N]^T$, based on the property in (2), the frequency band is defined as

$$\{\bar{\mathbf{v}}\}_{n-1} = \begin{cases} \bar{v}_n & n = 1 \text{ or } n = N - n + 2, \\ (\bar{v}_n, \bar{v}_{N-n+2}) & \text{else.} \end{cases} \quad (3)$$

When N is odd, the frequency bands are $(\bar{v}_1), (\bar{v}_2, \bar{v}_N), \dots, (\bar{v}_{\frac{N+1}{2}}, \bar{v}_{\frac{N+3}{2}})$; when N is even, they are $(\bar{v}_1), (\bar{v}_2, \bar{v}_N), \dots, (\bar{v}_{\frac{N+2}{2}})$. There are always $N_v = \lceil \frac{N+1}{2} \rceil$ frequency bands in all.

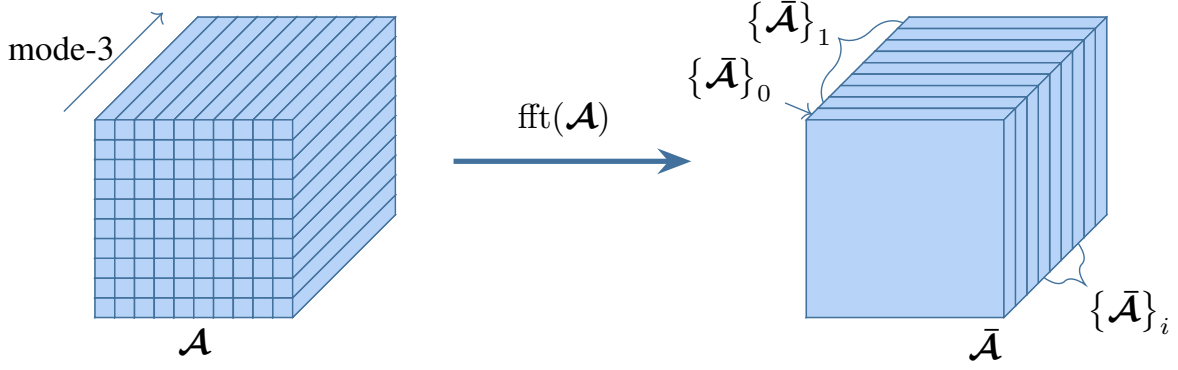


Fig. 2: Illustration about the DFT on a tensor.

Definition 2 (frequency component). For a vector $\mathbf{v} \in \mathbb{R}^N$, a frequency band $\{\bar{\mathbf{v}}\}_{n-1}$ in the Fourier domain can be transformed into a frequency component $[\mathbf{v}]_{n-1} \in \mathbb{R}^N$ in the time domain as follows

$$\begin{aligned} [\mathbf{v}]_{n-1} &= \text{ifft}(\{\bar{\mathbf{v}}\}_{n-1}) \\ &= \frac{1}{N} \mathbf{F}_N^H [0, \dots, 0, \bar{v}_n, 0, \dots, 0, \bar{v}_{N-n+2}, 0, \dots]^T \end{aligned}$$

Among all the components, the zero-frequency component $[\mathbf{v}]_0$ is

$$\begin{aligned} [\mathbf{v}]_0 &= \text{ifft}(\{\bar{\mathbf{v}}\}_0) \\ &= \left[\frac{1}{N} \sum_{n=1}^N v_n, \frac{1}{N} \sum_{n=1}^N v_n, \dots, \frac{1}{N} \sum_{n=1}^N v_n \right]^T \end{aligned} \quad (4)$$

It is distinctive because it assembles all the energy and indicates the average energy of a vector. For example, a vector $\mathbf{x} = [4, 6, 4, 6]^T$ has 3 frequency components $[\mathbf{x}]_0 = [5, 5, 5, 5]^T$, $[\mathbf{x}]_1 = [0, 0, 0, 0]^T$, and $[\mathbf{x}]_2 = [-1, 1, -1, 1]^T$ respectively. Intuitively, zero frequency component can be regarded as the average energy.

Lemma 1. A vector $\mathbf{v} \in \mathbb{R}^N$ can be represented as the sum of all frequency components.

$$\begin{aligned} \mathbf{v} &= \text{ifft}(\{\bar{\mathbf{v}}\}_0) + \text{ifft}(\{\bar{\mathbf{v}}\}_2) + \dots + \text{ifft}(\{\bar{\mathbf{v}}\}_{N_v-1}) \\ &= [\mathbf{v}]_0 + [\mathbf{v}]_1 + \dots + [\mathbf{v}]_{N_v-1} \end{aligned} \quad (5)$$

Consider a tensor $\mathcal{A} \in \mathbb{R}^{I_1 \times I_2 \times I_3}$, and $\bar{\mathcal{A}}$ as the result of the DFT along the third dimension of \mathcal{A} . The DFT and inverse DFT on a tensor can be represented as follows:

$$\bar{\mathcal{A}} = \text{fft}(\mathcal{A}, [], 3), \mathcal{A} = \text{ifft}(\bar{\mathcal{A}}, [], 3)$$

For convenience, we abbreviate it as $\bar{\mathcal{A}} = \text{fft}(\mathcal{A})$, $\mathcal{A} = \text{ifft}(\bar{\mathcal{A}})$ in this paper.

The concepts of frequency band and frequency component can be generalized to tensor data. Fig. 2 shows an illustration of the DFT on a tensor $\mathcal{A} \in \mathbb{R}^{I_1 \times I_2 \times I_3}$. $I_1 I_2$ DFTs need to be performed along the third mode, and $I = \lceil \frac{I_3+1}{2} \rceil$ frequency bands can be obtained. The transformation between frequency bands and frequency components is shown in Fig. 3.

Finally, a tensor can also be represented as the sum of its frequency components by Lemma 1 as follows:

$$\begin{aligned} \mathcal{A} &= \text{ifft}(\{\bar{\mathcal{A}}\}_0) + \text{ifft}(\{\bar{\mathcal{A}}\}_1) + \dots + \text{ifft}(\{\bar{\mathcal{A}}\}_{I-1}) \\ &= [\mathcal{A}]_0 + [\mathcal{A}]_1 + \dots + [\mathcal{A}]_{I-1} \end{aligned} \quad (6)$$

where $I = \lceil \frac{I_3+1}{2} \rceil$, and $[\mathcal{A}]_i, 0 \leq i \leq I-1$ represents the i -th frequency component of tensor \mathcal{A} .

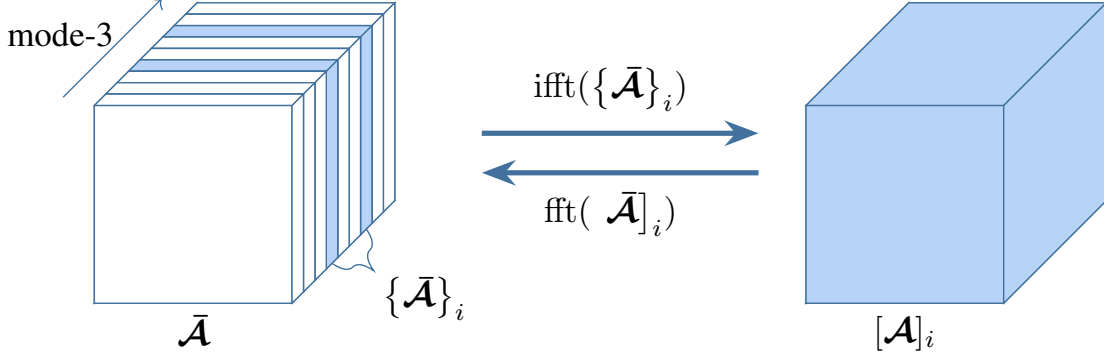


Fig. 3: Illustration of transformation between frequency band and frequency component

C. Preliminaries about *t*-SVD

For a tensor $\mathcal{A} \in \mathbb{R}^{I_1 \times I_2 \times I_3}$, define the unfold and fold operators of tensor as follows:

$$\text{unfold}(\mathcal{A}) = \begin{bmatrix} \mathcal{A}^{(1)} \\ \mathcal{A}^{(2)} \\ \vdots \\ \mathcal{A}^{(I_3)} \end{bmatrix}, \text{fold}(\text{unfold}(\mathcal{A})) = \mathcal{A}.$$

The block circular matrix $\text{bcirc}(\mathcal{A})$ and block diagonal matrix $\text{bdiag}(\mathcal{A})$ of \mathcal{A} are defined as follows:

$$\text{bcirc}(\mathcal{A}) = \begin{bmatrix} \mathcal{A}^{(1)} & \mathcal{A}^{(I_3)} & \dots & \mathcal{A}^{(2)} \\ \mathcal{A}^{(2)} & \mathcal{A}^{(1)} & \dots & \mathcal{A}^{(3)} \\ \vdots & \vdots & \ddots & \vdots \\ \mathcal{A}^{(I_3)} & \mathcal{A}^{(I_3-1)} & \dots & \mathcal{A}^{(1)} \end{bmatrix},$$

$$\text{bdiag}(\mathcal{A}) = \begin{bmatrix} \mathcal{A}^{(1)} & & & \\ & \mathcal{A}^{(2)} & & \\ & & \ddots & \\ & & & \mathcal{A}^{(I_3)} \end{bmatrix}$$

Definition 3 (*t*-product [35]). Given $\mathcal{A} \in \mathbb{R}^{I_1 \times I_2 \times I_3}$ and $\mathcal{B} \in \mathbb{R}^{I_2 \times I_4 \times I_3}$, the *t*-product between \mathcal{A} and \mathcal{B} is defined as follows:

$$\mathcal{C} = \mathcal{A} * \mathcal{B} = \text{fold}(\text{bcirc}(\mathcal{A}) \cdot \text{unfold}(\mathcal{B}))$$

where $\mathcal{C} \in \mathbb{R}^{I_1 \times I_4 \times I_3}$. When converted into Fourier domain, the *t*-product can be calculated by matrix product on each frontal slice separately as $\bar{\mathcal{C}}^{(i_3)} = \bar{\mathcal{A}}^{(i_3)} \bar{\mathcal{B}}^{(i_3)}$.

Definition 4 (conjugate transpose tensor [35]). The conjugate transpose of a tensor $\mathcal{A} \in \mathbb{R}^{I_1 \times I_2 \times I_3}$ is denoted as $\mathcal{A}^H \in \mathbb{R}^{I_2 \times I_1 \times I_3}$. We can get it by conjugate transposing each of the frontal slices and then reversing the order of the frontal slices from 2 to I_3 .

Definition 5 (identity tensor [35]). A tensor $\mathcal{I} \in \mathbb{R}^{I_1 \times I_1 \times I_3}$ is an identity tensor if its first frontal slice is an $I_1 \times I_1$ identity matrix and other slices are zero.

Definition 6 (orthogonal tensor [35]). A tensor \mathcal{Q} is called an orthogonal tensor if

$$\mathcal{Q}^H * \mathcal{Q} = \mathcal{Q} * \mathcal{Q}^H = \mathcal{I}$$

Definition 7 (F-diagonal tensor [35]). A tensor is called F-diagonal tensor if each of its frontal slice is a diagonal matrix.

Definition 8 (t-SVD [35]). For a tensor $\mathcal{A} \in \mathbb{R}^{I_1 \times I_2 \times I_3}$, the t-SVD of \mathcal{A} is :

$$\mathcal{A} = \mathcal{U} * \mathcal{S} * \mathcal{V}^H$$

where \mathcal{U} and \mathcal{V} are orthogonal tensors of size $I_1 \times I_1 \times I_3$ and $I_2 \times I_2 \times I_3$ respectively. $\mathcal{S} \in \mathbb{R}^{I_1 \times I_2 \times I_3}$ is an F -diagonal tensor.

Fig. 4 shows an illustration of the t-SVD. It can be easily calculated in the Fourier domain. We can get the frontal slices of $\bar{\mathcal{U}}, \bar{\mathcal{S}}, \bar{\mathcal{V}}$ by

$$\text{SVD}(\bar{\mathcal{A}}^{(i_3)}) = [\bar{\mathcal{U}}^{(i_3)}, \bar{\mathcal{S}}^{(i_3)}, \bar{\mathcal{V}}^{(i_3)}]$$

Definition 9 (tensor multi-rank [37]). The tensor multi-rank of a tensor $\mathcal{A} \in \mathbb{R}^{I_1 \times I_2 \times I_3}$ is defined as a vector whose i_3 -th entry equals to the matrix rank of the i_3 -th frontal slice in Fourier domain.

$$\text{rank}(\mathcal{A}) = [\text{rank}(\bar{\mathcal{A}}^{(1)}), \text{rank}(\bar{\mathcal{A}}^{(2)}), \dots, \text{rank}(\bar{\mathcal{A}}^{(I_3)})]^T$$

Definition 10 (tensor nuclear norm: TNN [39]). The tensor nuclear norm of a tensor \mathcal{A} based on t-SVD is defined as the average of nuclear norms of each its frontal slice in Fourier domain.

Based on t-SVD, TNN can be easily deduced as:

$$\begin{aligned} \|\mathcal{A}\|_{\text{TNN}} &= \frac{1}{I_3} \|\text{bcirc}(\mathcal{A})\|_* \\ &= \frac{1}{I_3} \|(\mathbf{F}_{I_3} \otimes \mathbf{I}_{I_1}) \cdot \text{bcirc}(\mathcal{A}) \cdot (\mathbf{F}_{I_3}^* \otimes \mathbf{I}_{I_2})\|_* \\ &= \frac{1}{I_3} \|\text{bdiag}(\bar{\mathcal{A}})\|_* = \frac{1}{I_3} \sum_{i_3=1}^{I_3} \|\bar{\mathcal{A}}^{(i_3)}\|_* \end{aligned} \quad (7)$$

D. Related Works

The basic assumption of RPCA problem is that the data matrix can be decomposed into a low-rank matrix \mathbf{L} and a sparse matrix \mathbf{E} , i.e., $\mathbf{X} = \mathbf{L} + \mathbf{E}$. Candes *et al.* [7] have proven that under some incoherent conditions, \mathbf{L} and \mathbf{E} can be recovered by solving the convex optimization problem as follows:

$$\underset{\mathbf{L}, \mathbf{E}}{\text{minimize}} \quad \|\mathbf{L}\|_* + \lambda \|\mathbf{E}\|_1 \quad \text{s.t.} \quad \mathbf{X} = \mathbf{L} + \mathbf{E}, \quad (8)$$

where $\|\cdot\|_*$ is the nuclear norm which represents the sum of singular values of low-rank matrix \mathbf{L} , $\|\cdot\|_1$ is ℓ_1 norm which represents the sum of absolute values of all entries in sparse matrix \mathbf{S} . The parameter λ is set to balance the two terms.

Robust tensor principal component analysis (RTPCA) assumes a tensor $\mathcal{X} \in \mathbb{R}^{I_1 \times I_2 \times I_3}$ can be formulated as

$$\mathcal{X} = \mathcal{L} + \mathcal{E}, \quad (9)$$

where \mathcal{L} is a low-rank tensor and \mathcal{E} is a sparse tensor. Several different nuclear norms for tensor have been proposed to solve the problem (9). Below are the details of these methods.

The Tucker decomposition based RTPCA can be formulated as follows [32]:

$$\underset{\mathcal{L}, \mathcal{E}}{\text{minimize}} \quad \sum_{d=1}^D \lambda_d \|\mathcal{L}^{\{d\}}\|_* + \|\mathcal{E}\|_1, \quad \text{s.t.} \quad \mathcal{X} = \mathcal{L} + \mathcal{E} \quad (10)$$

where $\mathcal{L}^{\{d\}}$ is the mode- d matricization of the low-rank tensor \mathcal{L} . For example, when given a order-3 tensor, it uses the combination of three matrix nuclear norms to solve the Tucker rank minimization problem.

Based on t-SVD, a new tensor nuclear norm (TNN) is rigorously deduced, and the corresponding convex optimization model (RTPCA-TNN) is given as follows [39]:

$$\underset{\mathcal{L}, \mathcal{E}}{\text{minimize}} \quad \|\mathcal{L}\|_{\text{TNN}} + \lambda \|\mathcal{E}\|_1, \quad \text{s.t.} \quad \mathcal{X} = \mathcal{L} + \mathcal{E}. \quad (11)$$

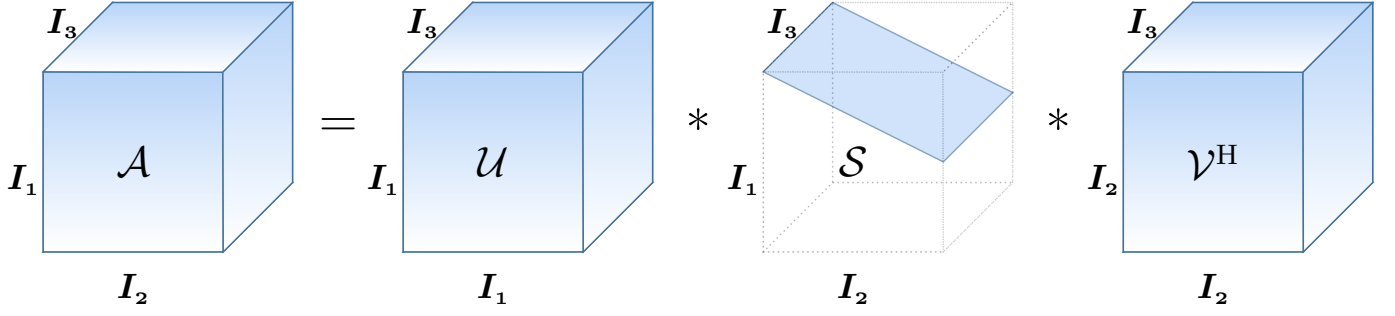


Fig. 4: Illustration of t-SVD of a tensor $\mathcal{A} \in \mathbb{R}^{I_1 \times I_2 \times I_3}$

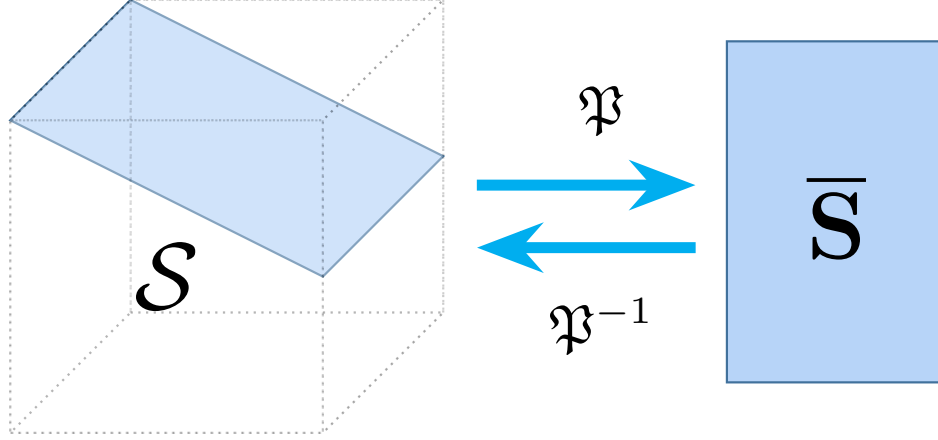


Fig. 5: Illustration of transforms between core tensor $\mathcal{S} \in \mathbb{R}^{I_1 \times I_2 \times I_3}$ and core matrix $\bar{\mathcal{S}} \in \mathbb{R}^{\min\{I_1, I_2\} \times I_3}$

where λ is a regularization parameter, and suggested to be set as $1/\sqrt{\max(I_1, I_2)I_3}$ to guarantee the exact recovery. $\|\mathcal{L}\|_{\text{TNN}}$ is the TNN for the low-rank tensor \mathcal{L} (see the definition in Section III). It has been proven that the low-rank tensor and the sparse tensor can be perfectly recovered under some certain tensor incoherence conditions. The RTPCA-TNN method has been applied to solve the image recovery and background modeling problem successfully.

To further exploit the low-rank structures in multi-way data, the improved tensor nuclear norm (ITNN) is proposed, and defined as the weighted sum of TNN and nuclear norm of core matrix as follows [42]:

$$\|\mathcal{X}\|_{\text{ITNN}} = \|\mathcal{X}\|_{\text{TNN}} + \lambda_S \|\bar{\mathcal{S}}\|_* \quad (12)$$

where λ_S is set to balance the two terms. Fig. 5 shows how to obtain the core matrix from the core tensor. Accordingly, a new ITNN-RTPCA method can be obtained:

$$\underset{\mathcal{L}, \mathcal{E}}{\text{minimize}} \|\mathcal{L}\|_{\text{ITNN}} + \lambda \|\mathcal{E}\|_1, \text{ s.t. } \mathcal{X} = \mathcal{L} + \mathcal{E}. \quad (13)$$

III. METHOD

A. Frequency Components Analysis (FCA)

The existing RTPCA methods based on t-SVD only take the Fourier transform to connect the first two modes with the third mode of a tensor. The intrinsic properties on Fourier domain have not been utilized sufficiently. While the existing TNN-related methods treat all the frequency bands equally in the Fourier domain and shrink them with a same threshold. It is inappropriate and inflexible to deal with various tensor data in such a way, which makes prior knowledge about Fourier analysis neglected.

According to the analysis results about the Fourier transform in section II-B, when we take the DFT along the third mode of a order-3 tensor, many frequency bands in the Fourier domain can be obtained and each frequency

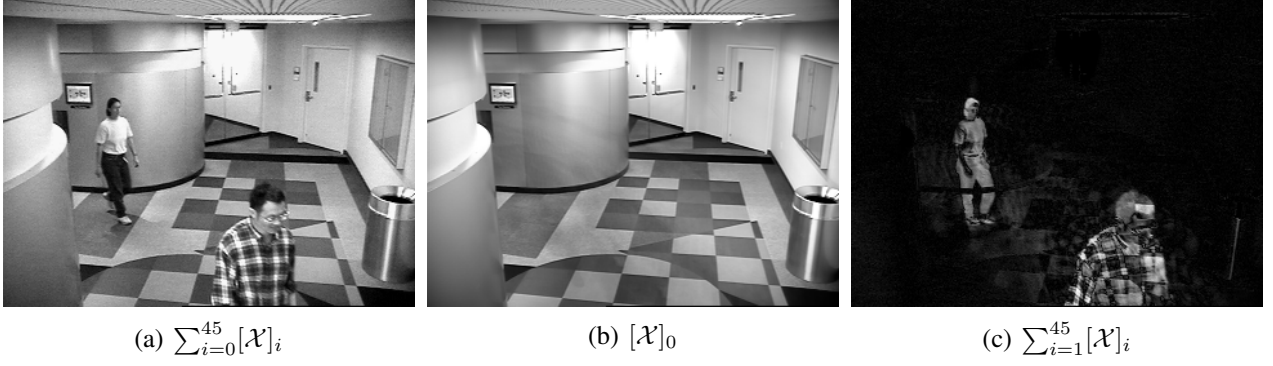


Fig. 6: FCA results of a grayscale video $\mathcal{X} \in \mathbb{R}^{320 \times 240 \times 90}$. (a) Original; (b) zero frequency component; (c) non-zero frequency components.

band corresponds to a frequency component in the time domain. In other words, given a tensor $\mathcal{X} \in \mathbb{R}^{I_1 \times I_2 \times I_3}$, it can be decomposed into I frequency components via Fourier analysis:

$$\mathcal{X} = [\mathcal{X}]_0 + [\mathcal{X}]_1 + \cdots + [\mathcal{X}]_{I-1} \quad (12),$$

where $I = \lceil \frac{I_3+1}{2} \rceil$.

We select a grayscale surveillance video sequence from SBI dataset [47]. It has 90 frames with size 320×240 , denoted as $\mathcal{X} \in \mathbb{R}^{320 \times 240 \times 90}$. There are $I = 46$ frequency bands in Fourier domain, and we analyze the corresponding 46 frequency components in the time domain. Fig. 6 is an illustration of the frequency component analysis (FCA) results for this grayscale video. We can see that the zero-frequency component contains almost all of the background information (low-rank component), and the moving object (sparse component) lies in the nonzero-frequency component.

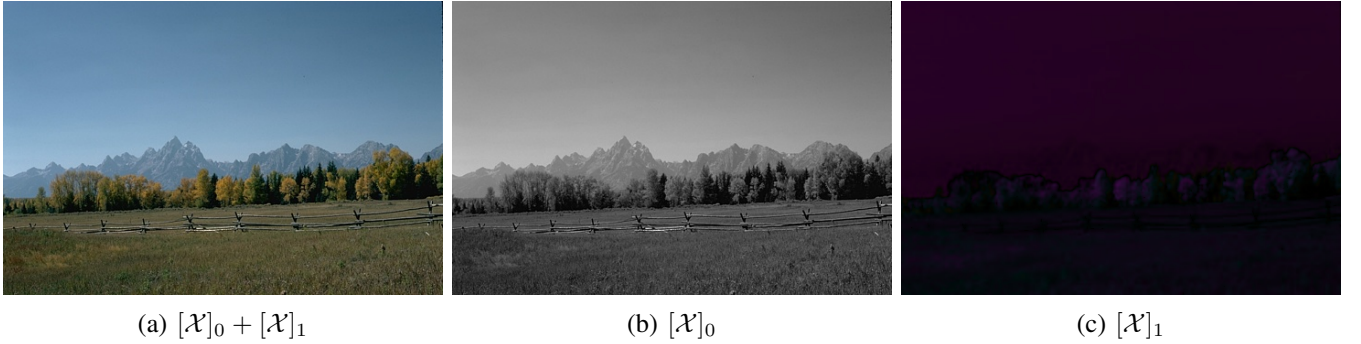


Fig. 7: FCA results of a color image $\mathcal{X} \in \mathbb{R}^{321 \times 481 \times 3}$. (a) original; (b) zero-frequency component; (c) nonzero-frequency component.

In addition, a color image of size 321×481 is randomly selected from Berkeley Segmentation Dataset [48], denoted as $\mathcal{X} \in \mathbb{R}^{321 \times 481 \times 3}$. There are two frequency components including zero frequency component and non-zero frequency component. Fig. 7 shows the FCA results for this color image. As we can see, the zero frequency component contains the main texture information, and the nonzero frequency component contains the difference information of three channels. Therefore, we can conclude that different bands should be treated differently.

Motivated by the above analysis of the visual data, we can see that the classical TNN defined by t-SVD is not appropriate in some applications, and different weights should be assigned to different frequency bands. With the newly defined frequency weighted TNN, the low-rank components will be extracted more completely.

B. Frequency-weighted Tensor Nuclear Norm (FTNN)

In order to better extract low-rank structure, we define the frequency-weighted tensor nuclear norm (FTNN) of a tensor $\mathcal{X} \in \mathbb{R}^{I_1 \times I_2 \times I_3}$ as follows:

$$\begin{aligned} \|\mathcal{X}\|_{\text{FTNN}} &= \frac{1}{I_3} \|\text{bcirc}(\mathcal{X})\|_{\text{FTNN}} = \frac{1}{I_3} \|\text{bdiag}(\bar{\mathcal{X}})\|_{\text{FTNN}} \\ &= \frac{1}{I_3} \left\| \begin{bmatrix} \alpha_1 \bar{\mathcal{X}}^{(1)} & & & \\ & \alpha_2 \bar{\mathcal{X}}^{(2)} & & \\ & & \ddots & \\ & & & \alpha_{I_3} \bar{\mathcal{X}}^{(I_3)} \end{bmatrix} \right\|_* \\ &= \frac{1}{I_3} \sum_{i_3=1}^{I_3} \alpha_{i_3} \|\bar{\mathcal{X}}^{(i_3)}\|_* \end{aligned} \quad (14)$$

where $\alpha_{i_3} \geq 0$ is called frequency weight or filtering coefficient.

According to the property in (2), we can get $\alpha_i = \alpha_{I_3-i+2}$, $i = 2, 3, \dots, I$, where $I = \lceil \frac{I_3+1}{2} \rceil$. We need to choose I weights, which form a frequency-weighted vector $\alpha = [\alpha_1, \alpha_2, \dots, \alpha_I]^T$. When $\alpha_1 = \alpha_2 = \dots = \alpha_I = 1$, the FTNN reduces to TNN. The value of weighted vector α depends on the prior knowledge of Fourier analysis in applications, which can be adjusted to achieve filtering in the Fourier domain. Different from existing definitions of TNN, the FTNN is the first one defined via Fourier analysis, and it is very practical due to the wide application of frequency analysis.

Similar to tensor singular value thresholding (TSVT) operator related to TNN [39], the frequency-weighted tensor singular value thresholding (FTSVT) are strictly derived. The optimization model for proximal mapping is as follows:

$$\min_{\mathcal{X}} \tau \|\mathcal{X}\|_{\text{FTNN}} + \frac{1}{2} \|\mathcal{X} - \mathcal{Y}\|_{\text{F}}^2 \quad (15)$$

It is equivalent to

$$\begin{aligned} &\min_{\mathcal{X}} \tau \|\mathcal{X}\|_{\text{FTNN}} + \frac{1}{2I_3} \|\bar{\mathcal{X}} - \bar{\mathcal{Y}}\|_{\text{F}}^2 \\ &\Leftrightarrow \min_{\mathcal{X}} \tau \|\text{bdiag}(\bar{\mathcal{X}})\|_{\text{FTNN}} + \frac{1}{2I_3} \|\bar{\mathcal{X}} - \bar{\mathcal{Y}}\|_{\text{F}}^2 \\ &\Leftrightarrow \min_{\mathcal{X}} \frac{1}{I_3} \sum_{i_3=1}^{I_3} \left(\tau \alpha_{i_3} \|\bar{\mathcal{X}}^{(i_3)}\|_* + \frac{1}{2} \|\bar{\mathcal{X}}^{(i_3)} - \bar{\mathcal{Y}}^{(i_3)}\|_{\text{F}}^2 \right) \end{aligned} \quad (16)$$

For the matrix data, we have the singular values thresholding operator (SVT) [16], [49]:

$$\mathbf{U}(\mathbf{S} - \tau)_+ \mathbf{V}^T = \arg\min_{\mathbf{X}} \tau \|\mathbf{X}\|_* + \frac{1}{2} \|\mathbf{X} - \mathbf{Y}\|_{\text{F}}^2, \quad (17)$$

where $(x - \tau)_+ = \max(x - \tau, 0)$ and $\mathbf{Y} = \mathbf{U} \cdot \mathbf{S} \cdot \mathbf{V}$.

Therefore, the problem in (15) can be divided into I_3 subproblems, and each subproblem can be solved by (17). We can get

$$\text{FTSVT}_{\alpha\tau}(\mathcal{Y}) = \arg\min_{\mathcal{X}} \tau \|\mathcal{X}\|_{\text{FTNN}} + \frac{1}{2} \|\mathcal{X} - \mathcal{Y}\|_{\text{F}}^2 \quad (18)$$

The computational details about FTSVT operator are given in Algorithm 1. Notice that when $\bar{\mathcal{R}}^{(i)} = 0$, the i -th frequency band $\{\bar{\mathcal{R}}\}_{i-1}$ is totally preserved, and this frequency band is totally discarded for $\bar{\mathcal{R}}^{(i)} = +\infty$. We do not need to compute SVD at this point.

Although the definition of the proposed FTNN is just to set a series of weights on the frontal slices in the Fourier domain, each weight has its explicit physical background in the Fourier domain. This makes the used weights different from existing data-driven works which set the weights for singular values by an updating rule iteratively. The FCA of the tensor data in the third mode makes the t-SVD based RTPCA be enhanced by its physical background.

Algorithm 1 FTSVT operator

Input: Tensor $\mathcal{X} \in \mathbb{R}^{I_1 \times I_2 \times I_3}$, Weighted vector α , Threshold τ

Compute $\bar{\mathcal{X}} = \text{fft}(\mathcal{X})$

for $i = 1, \dots, \lceil \frac{I_3+1}{2} \rceil$ **do**

if $\alpha_i = 0$ **then**

$\bar{\mathcal{R}}^{(i)} = \bar{\mathcal{X}}^{(i)}$

else if $\alpha_i = \infty$ **then**

$\bar{\mathcal{R}}^{(i)} = 0$

else

$[\mathbf{U}, \mathbf{S}, \mathbf{V}] = \text{SVD}(\bar{\mathcal{X}}^{(i)})$

$\bar{\mathcal{R}}^{(i)} = \mathbf{U} \cdot (\mathbf{S} - \alpha_i \tau)_+ \cdot \mathbf{V}^T$

end if

end for

for $i = \lceil \frac{I_3+1}{2} \rceil + 1, \dots, I_3$ **do**

$\bar{\mathcal{R}}^{(i)} = \text{conj}(\bar{\mathcal{R}}^{(I_3-i+2)})$

end for

$\mathcal{R} = \text{ifft}(\bar{\mathcal{R}})$

Output: Reconstruction tensor \mathcal{R}

Here we only focus on the case for order-3 tensor. As for higher-order tensors like color video, the multi-dimensional Fourier transform can be used to deal with these problems.

C. Frequency-weighted RTPCA

The convex optimization model for RTPCA with the proposed FTNN can be formulated as follows:

$$\min_{\mathcal{L}, \mathcal{E}} \|\mathcal{L}\|_{\text{FTNN}} + \lambda \|\mathcal{E}\|_1, \text{ s.t. } \mathcal{X} = \mathcal{L} + \mathcal{E}. \quad (19)$$

where $\mathcal{X} \in \mathbb{R}^{I_1 \times I_2 \times I_3}$ is the observed tensor, and it can be decomposed into a low-rank tensor \mathcal{L} and a sparse tensor \mathcal{E} . λ is a regular parameter that is used to balance the two terms.

The alternating direction method of multiplier (ADMM) can be applied to solve the convex optimization model (19) [50]. The corresponding augmented Lagrangian function is:

$$\begin{aligned} \Gamma(\mathcal{L}, \mathcal{E}, \mathcal{Y}, \mu) = & \|\mathcal{L}\|_{\text{FTNN}} + \lambda \|\mathcal{E}\|_1 + \langle \mathcal{Y}, \mathcal{X} - \mathcal{L} - \mathcal{E} \rangle \\ & + \frac{\mu}{2} \|\mathcal{X} - \mathcal{L} - \mathcal{E}\|_F^2 \end{aligned} \quad (20)$$

where \mathcal{Y} is dual variable and μ is penalty parameter. Its optimization can be divided into three subproblems, including low-rank component approximation, sparse component minimization and dual variable update.

In the k -th iteration, the subproblem about the low-rank component \mathcal{L} can be solved by the FTSVT operator as follows:

$$\begin{aligned} \mathcal{L}_{k+1} = & \underset{\mathcal{L}}{\text{argmin}} \|\mathcal{L}\|_{\text{FTNN}} + \frac{\mu_k}{2} \|\mathcal{L} - \mathcal{X} + \mathcal{E}_k - \frac{\mathcal{Y}_k}{\mu_k}\|_F^2, \\ = & \text{FTSVT}_{\frac{\alpha_k}{\mu_k}}(\mathcal{X} - \mathcal{E}_k + \frac{\mathcal{Y}}{\mu_k}) \end{aligned} \quad (21)$$

Because all the tensor norms used in our optimization model can be calculated slices-wisely on the third mode. This t-SVD based RTPCA problem can be divided into I_3 matrix robust PCA problems in the Fourier domain.

Algorithm 2 ADMM for FTNN-RTPCA

Input: Tensor $\mathcal{X} \in \mathbb{R}^{I_1 \times I_2 \times I_3}$, weighted vector α , parameter λ .

Initialize: $\mathcal{L} = \mathcal{E} = \mathcal{Y} = 0$, μ , ρ , ε

while not converged **do**

1. Update $\mathcal{L}_{k+1} = \text{FTSVT}_{\frac{\alpha_k}{\mu_k}}(\mathcal{X} - \mathcal{E}_k - \frac{\mathcal{Y}_k}{\mu_k})$
2. Update $\mathcal{E}_{k+1} = \text{sth}_{\frac{\lambda}{\mu_k}}(\mathcal{X} - \mathcal{L}_{k+1} - \frac{\mathcal{Y}_k}{\mu_k})$
3. Update $\mathcal{Y}_{k+1} = \mathcal{Y}_k + \mu_k(\mathcal{L}_{k+1} + \mathcal{E}_{k+1} - \mathcal{X})$
4. Update $\mu_{k+1} = \rho\mu_k$
5. Update α_{k+1}
6. Check condition : $\|\mathcal{L}_{k+1} - \mathcal{L}_k\|_F / \|\mathcal{L}_k\|_F \leq \varepsilon$

end while

Output: \mathcal{L} , \mathcal{E}

The sparse component subproblem can be solved by

$$\begin{aligned} \mathcal{E}_{k+1} &= \underset{\mathcal{E}}{\operatorname{argmin}} \lambda \|\mathcal{E}\|_1 + \frac{\mu_k}{2} \|\mathcal{L}_{k+1} + \mathcal{E} - \mathcal{X} - \frac{\mathcal{Y}_k}{\mu_k}\|_F^2 \\ &= \text{sth}_{\frac{\lambda}{\mu_k}}(\mathcal{X} - \mathcal{L}_{k+1} + \frac{\mathcal{Y}_k}{\mu_k}) \end{aligned} \quad (22)$$

where $\text{sth}_\tau(\mathcal{X})$ represents the entry-wise soft thresholding operator. It means that for any entries x in \mathcal{X} we have

$$\text{sth}_\tau(x) = \operatorname{sgn}(x) \max(|x| - \tau, 0) \quad (23)$$

Finally, we update the dual variable \mathcal{Y}_k as follows:

$$\mathcal{Y}_{k+1} = \mathcal{Y}_k + \mu_k(\mathcal{X} - \mathcal{L}_{k+1} - \mathcal{E}_{k+1}) \quad (24)$$

After updating these three terms, the frequency weighting vector α needs to be updated accordingly, and the updating rule will be discussed in Section IV-A1 for different applications. In addition, we set the parameter $\lambda = 1/\sqrt{\max(I_1, I_2)I_3}$ as it is recommended in [39]. Algorithm 2 provides the details of the whole procedure for frequency-weighted robust tensor principal component analysis (FTNN-RTPCA) method.

D. Computational complexity

Most computational costs of Algorithm 2 lie in the update of low-rank components. Given an observed tensor $\mathcal{X} \in \mathbb{R}^{I_1 \times I_2 \times I_3}$, the frequency-weighted vector is $\alpha = [\alpha_1, \alpha_2, \dots, \alpha_I]^T$ where $I = \lceil \frac{I_3+1}{2} \rceil$. When the number of elements $0 < \alpha_k < +\infty$ is P , we need perform $I_1 I_2$ FFTs and P SVDs at each iteration. When updating the low-rank component \mathcal{L} , the computational cost in each iteration is $O(I_1 I_2 I_3 \log I_3 + P I_{\max} I_{\min}^2)$, where $I_{\max} = \max(I_1, I_2)$, $I_{\min} = \min(I_1, I_2)$ and $0 \leq P \leq I = \lceil \frac{I_3+1}{2} \rceil$. When updating the sparse component \mathcal{E} , we need to compute the soft-thresholding operation in (22) and the cost is $O(I_1 I_2 I_3)$. Above all, the computational complexity of FTNN-RTPCA is $O(I_1 I_2 I_3 (\log I_3 + 1) + P I_{\max} I_{\min}^2)$. Compared to RTPCA [39] whose costs in each iteration is $O(I_1 I_2 I_3 (\log I_3 + 1) + P I_{\max} I_{\min}^2)$, the computational complexity for the proposed FTNN-RTPCA method is less than or equal to the classical RTPCA method [39].

In Section IV, we will show that in some selected applications, P can be reduced to 0, which results in an SVD-free version of the proposed FTNN-RTPCA. Therefore, the processing time is greatly reduced.

IV. EXPERIMENTS RESULTS

To verify the performance of the proposed FTNN, we conduct three numerical experiments in this section. First, we do some simulation experiments on the synthetic 3D data to demonstrate the difference between TNN and FTNN. Specially, the setting of frequency-weighted vector is analyzed in detail, then real color image denoising

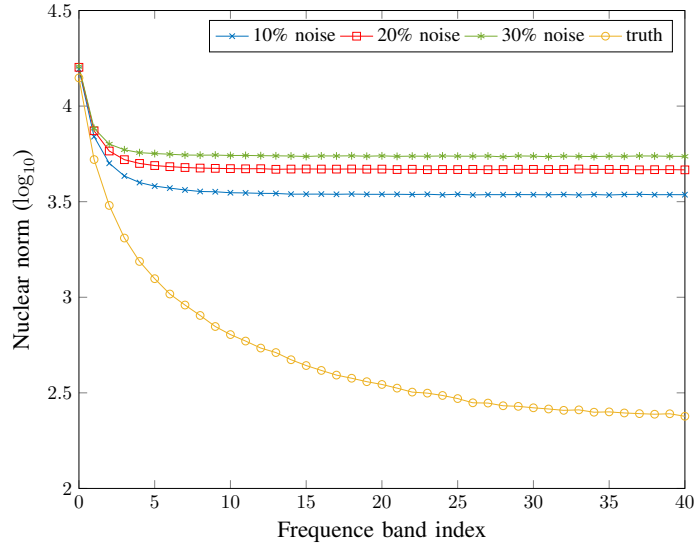


Fig. 8: Nuclear norm distribution of frequency band for the synthetic data under different sparse noises.

experiments are conducted and some other RPCA-based algorithms are selected to compare with our FTNN-RTPCA. Finally, the proposed FTNN-RTPCA is applied to the background modeling from surveillance video sequences. we compare our FTNN-RTPCA with some other state-of-the-art methods which are based on low-rank and sparse modeling. All experiments are conducted using MatLab R2014b software on an Intel CPU i5-6300 HQ and 8GB RAM computer.

A. Synthetic 3D data

The synthetic 3D data is generated by utilizing MATLAB function `phantom3d`¹. Each frontal slice of this synthetic data consists of some simple ellipsoids. As the ellipsoids for each frontal slice only change slightly, all frontal slices are very similar and can be regarded as the low-rank component. When it is corrupted by some sparse noise, the proposed FTNN-RTPCA method can be used to recover the clean original data. According to the FCA results in section III-A, when the corrupted data is converted to the Fourier domain, the changes of ellipsoids and the sparse noise will mainly lie in non-zero frequency components. The task of this experiment is to remove the sparse noise, recover the clean synthetic 3D data including the change information and details as much as possible.

1) *The Setting of Frequency-Weighted Vector*: The value of the frequency-weighted vector α plays a vital role in our FTNN-RTPCA method, which depends on the prior knowledge of data in the Fourier domain. α_k varies with respect to frequency bands and should be determined by the real physical significance of different frequency bands or frequency components. In general, the zero-frequency component contains the main information of low-rank component and other frequency components also have different information. Therefore, in order to avoid information loss on each frontal slice of the tensor, α_1 with respect to zero-frequency component should be set to a small value while we should also assign relatively large and different weights to the non-zero components.

For better illustrating the influence of the sparse noise on different frequency bands, we analyze the nuclear norm for different frequency bands of the synthetic data under different sparse noises. The size of the clean synthetic data is $200 \times 200 \times 80$ and there will be 41 frequency bands after applying DFT on the third mode. The corrupted ratio $R_s = 30\%$ means 30% pixels of the clean data are randomly selected to be random values in $[0, 255]$. The order-3 clean tensor is corrupted with 10%, 20%, 30% sparse noise respectively. Then we calculate the nuclear norms of 41 frequency bands of these corrupted data in the Fourier domain. Fig. 8 shows the results.

As we can see from Fig. 8, the uncorrupted tensor enjoys a rapid decay of the nuclear norms on the third mode which means information are more intensive in the low frequency bands. And the greater the corrupted ratio, the larger the deviation of the nuclear norm of each frequency band which means the more each band will be affected. On the other hand, whatever the corrupted ratio, it can be seen that sparse noise has little effect on

¹<https://www.mathworks.com/matlabcentral/fileexchange/50974-3d-shepp-logan-phantom>

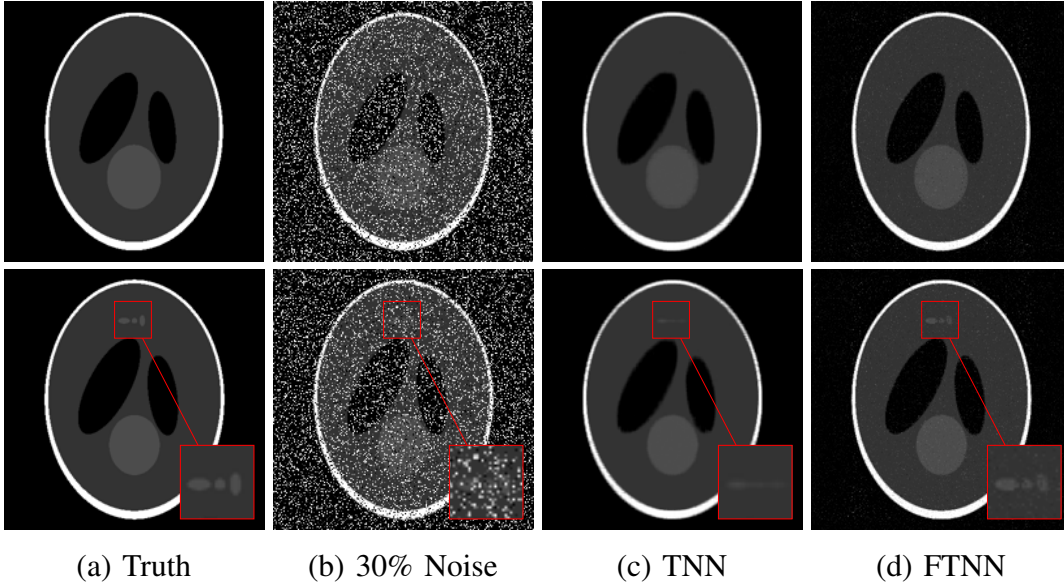


Fig. 9: Recovery results of TNN and FTNN method on synthetic 3D data. The top and bottom are the results of frame 1 and 11, respectively.

the zero frequency component and the higher band is more likely to be affected by the noise as the nuclear norm changes more. Therefore, we consider assigning greater weights to higher frequency bands to ensure better recovery performance. Suppose a tensor $\mathcal{X} \in \mathbb{R}^{I_1 \times I_2 \times I_3}$, which has $\lceil \frac{I_3+1}{2} \rceil$ frequency bands, we adopt the updating rule of the weighted vector $\alpha = [\alpha_1, \alpha_2, \dots, \alpha_{I_3}]^T$ as:

$$\alpha_k = \frac{C_k^1}{iter} + C_k^2, \quad 1 \leq k \leq \left\lceil \frac{I_3 + 1}{2} \right\rceil. \quad (25)$$

where $iter$ represents the $iter$ -th iteration in algorithm 2, C_k^1 and C_k^2 are pre-defined superparameters. α_k is set to be related to the number of iteration because the bands differ in each iteration.

With adjusting the values of C_k^1 and C_k^2 , the frequency band is controlled to be suppressed or preserved. When solving the low-rank approximation subproblem in (21), we set $\alpha_m = C_m^1 = C_m^2 = 0$ to keep the m -th frequency band entirely and $\alpha_n = C_n^1 = C_n^2 = +\infty$ will mean the n -th frequency band is set as zero and is discarded in each iteration. A less weighted value will mean that this band is to be retained more.

2) *Simulated Experiments:* In order to verify the performance of the FTNN-RTPCA algorithm, we conduct the synthetic 3D data denoising experiment in this section. The size of the original clean synthetic 3D data is $200 \times 200 \times 21$. \mathcal{X} represents the corrupted data with $R_s = 30\%$ and there are 11 frequency bands. The task is to recover the clean low-rank component from the corrupted tensor \mathcal{X} . Here we use Peak Signal-to-Noise Ratio (PSNR) and relative square error (RSE) to evaluate the recovery accuracy. When $\hat{\mathcal{L}} \in \mathbb{R}^{I_1 \times I_2 \times I_3}$ represents the recovered tensor and the original data is denoted by $\mathcal{L}_0 \in \mathbb{R}^{I_1 \times I_2 \times I_3}$, PSNR and RSE are defined as:

$$\begin{aligned} \text{PSNR} &= 10 \log_{10} \left(\frac{I_1 I_2 I_3 \|\mathcal{L}_0\|_\infty^2}{\|\hat{\mathcal{L}} - \mathcal{L}_0\|_F^2} \right) \\ \text{RSE} &= \frac{\|\hat{\mathcal{L}} - \mathcal{L}_0\|_F}{\|\mathcal{L}_0\|_F} \end{aligned} \quad (26)$$

We compare the proposed FTNN-RTPCA with TNN-RTPCA [39]. For fairness, the parameter is set to the same values as $\lambda = \sqrt{\max(I_1, I_2)I_3}$. To preserve the details and the texture information as much as possible, we set the weighting vector α as:

$$\alpha = [0.3, 0.5, 0.6, 0.75, 0.9, 1, 1.05, 1.05, 1.1, 1.1, 1.1]^T \quad (27)$$

where lower frequency bands are assigned smaller weights to avoid information loss and make a balance between

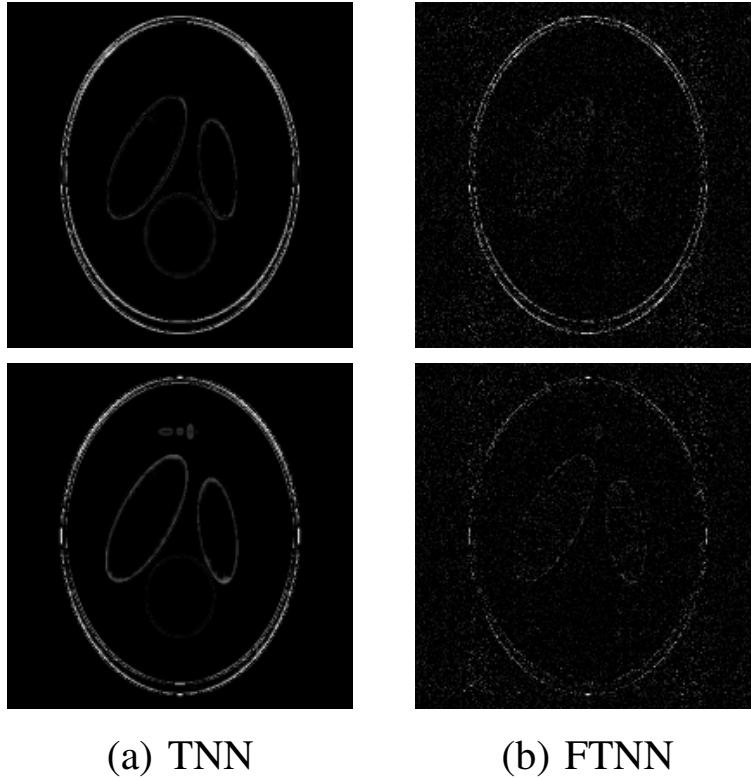


Fig. 10: Information loss of TNN and FTNN on two frames. The top and bottom are the results of frame 1 and 11, respectively.

noise and the details for different bands.

TABLE I: Comparison of TNN and FTNN in terms of PSNE and RSE on synthetic 3D data

	FTNN	TNN
PSNR	31.1040	27.7939
RSE	0.1149	0.1696

Fig. 9 shows the recovery results of our proposed FTNN and the classical TNN method on synthetic 3D data when the corrupted ratio is 30%. At the same time, defined as $|\hat{\mathcal{L}} - \mathcal{L}_0|$, the information loss for the frames 1 and 11 are presented in Fig. 10. As we can see, TNN can remove the sparse noise well but regards the changes between different frontal slices as sparse components and removes them together, which would lead to large information loss of the original clean data. However, FTNN can keep these texture information from being removed as sparse components.

In addition, the comparison of PSNR and RSE between TNN and FTNN are shown in Table I. The proposed FTNN method has the better recovery accuracy performance compared with TNN. We can conclude that based on the prior knowledge of the data in the frequency domain, FTNN can adjust the frequency-weighted vector to remove the sparse noise while retaining the change information along the third dimension. Therefore, the proposed FTNN is more flexible and efficient for denoising tasks compared with TNN.

In the end, we analyze the nuclear norms of frequency bands for different recovery results. As Fig. 11 shows, the nuclear norm distribution for the proposed FTNN method is more approximate the true distribution while TNN works badly. It can be further illustrated that FTNN achieves better recovery performance than TNN.

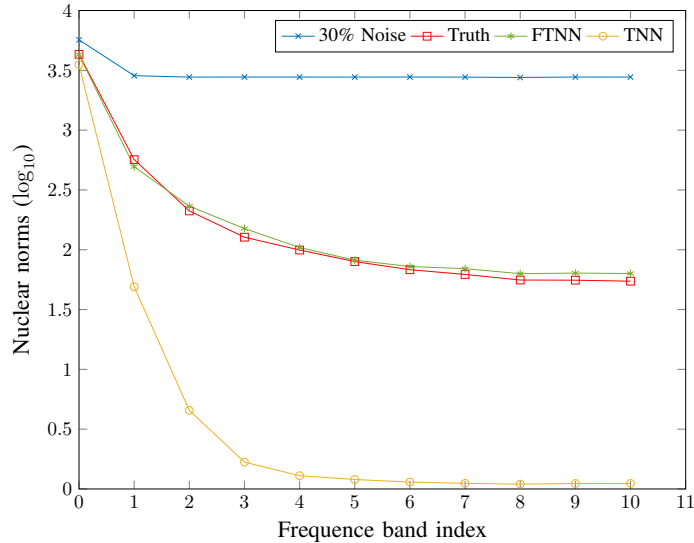


Fig. 11: Nuclear norm distribution with respect to frequency band for the recovery results of TNN and FTNN.

B. Color Image Denoising

A color image has three channels which possess strong correlation on the third mode. Since each channel of an image can be approximated by a low-rank matrix [51], it can be regarded as a low-rank tensor. In real world, images always suffer from sparse noise. In this section, we apply the proposed FTNN method to solve the color image denoising problem.

Fifty color images are chosen randomly from the Berkeley Segmentation Dataset [48] for this group of experiments. For every color image, we randomly choose 10% and 20% pixels and set their values as random values in the range [0,255]. To verify the performance of our FTNN method, we select some other state-of-the-art methods for comparison including RPCA [7], SNN [32], TNN [39]. RPCA is a matrix-based method while the others are tensor-based methods. Suppose the size of the corrupted image is $I_1 \times I_2 \times 3$, we set $\lambda = 1/\sqrt{\max(I_1, I_2)}$ for RPCA and $\lambda = [15, 15, 1.5]^T$ for SNN. As for TNN and the proposed FTNN, the parameter λ is set to be $\sqrt{3 \times \max(I_1, I_2)}$.

As analyzed in Section III-A, a color image have two frequency components. The main texture information is shown in the zero frequency component when nonzero frequency component only contains the difference information of three channels. On the other hand, it has been shown in Section IV-A1 that the influence of sparse noise on non-zero frequency component is relatively large and higher noise corrupted ratio will have a greater impact on each frequency component. In order to better recover the true color image information, we set the weighting vector $\alpha = [\alpha_1, \alpha_2]^T$ for FTNN as :

$$\begin{aligned} 10\% \text{ Noise} : \alpha &= [0.35, 1]^T \\ 20\% \text{ Noise} : \alpha &= \left[\frac{0.85}{iter} + 0.45, 1 \right]^T \end{aligned} \quad (28)$$

TABLE II: Comparison of recovery performance for varying noises on color images.

Corrupted Ratio	Indicators	RPCA	SNN	TNN	FTNN
10%	PSNR	25.8731	26.8047	28.6684	35.2650
	RSE	0.12363	0.11017	0.08834	0.04117
20%	PSNR	24.5125	25.4716	26.8288	30.1411
	RSE	0.14331	0.12783	0.10880	0.07431

We use PSNR and RSE to evaluate the recovery performance of these methods. Table II shows the average value of two metrics of 50 examples with different methods under varying noises. It shows that the proposed FTNN method obtains the highest PSNR values and the lowest RSE value. We can conclude that FTNN achieves the best

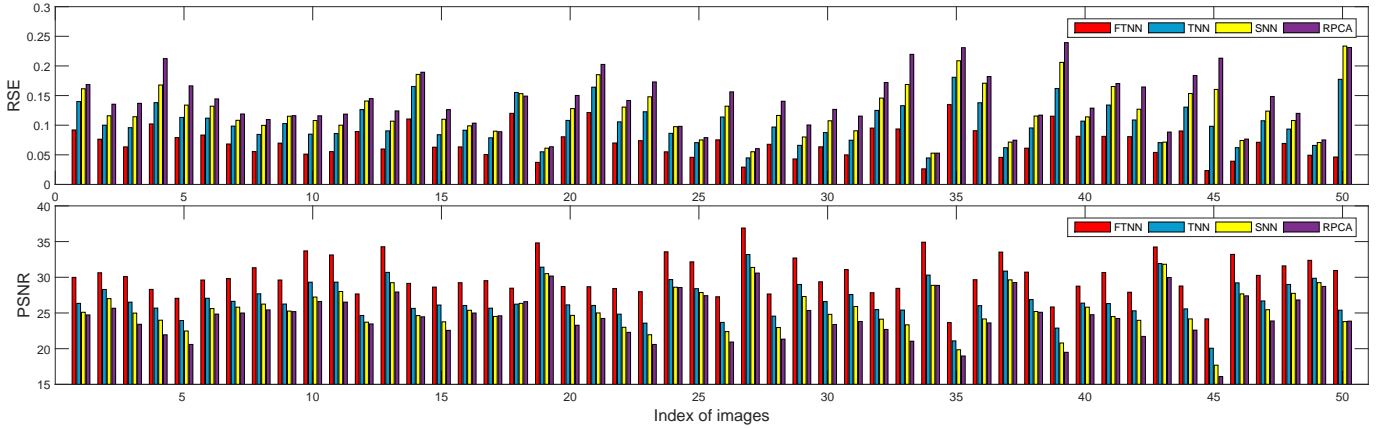


Fig. 12: Comparison of PSNR and RSE with 20% noise

recovery performance. In addition, we present the comparison results of different methods in terms of PSNR and RSE for 50 groups of experiments when the corrupted ratio is 20% in Fig. 12. We can see that our FTNN always achieve the highest recovery accuracy.

Fig. 13 shows the results of five examples, which are animal, house, child, flower and person, respectively. It can be seen that the recovery images by RPCA, SNN, TNN methods are relatively fuzzy while the proposed FTNN can obtain the best recovery images. In particular, the results of FTNN are very clear in details such as the crosses on the roof and the stamens of the flowers.

Based on the above comparison, we summarize several conclusions. First, RPCA gets the worst recovery performance because it processes each channel separately and the relevant information about three channels are ignored. Secondly, FTNN and TNN can obtain better results compared with RPCA and SNN. The reason is that the t-SVD framework make more efficient use of the multi-dimensional structure of the data. Finally, the proposed FTNN can achieve the best performance and recover more details because each band is treated differently.

Since the frequency-weighted vector is chosen according to the prior knowledge of the data in the Fourier domain, more details have been recovered in the results by FTNN method. Therefore, FTNN is an efficient and flexible algorithm to perform well by designing an appropriate weighted vector.

C. Background Modeling

In this section, we apply the proposed FTNN method to solve the background modeling problem. The task of background modeling is to get a good and clean background also known as the foreground-free image from a video sequence. This is a pre-process step in many visual applications such as surveillance video processing, object direction and segmentation. The RPCA-related methods can be used to solve this problem because of the strong correlations between frames.

To verify performance of our FTNN method in this experiment, we select five color video sequences from dataset SBI [47]. They are CAVIAR1 sequences with 150 frames of size $384 \times 256 \times 3$, HumanBody2 sequences with 93 frames of size $320 \times 240 \times 3$, HighwayI sequences with 88 frames of size $320 \times 240 \times 3$, HighwayII sequences with 100 frames of size $320 \times 240 \times 3$ and IBMTes2 sequences with 90 frames of size $320 \times 240 \times 3$. For comparison, we choose four methods. They are matrix-based method RPCA, tensor-based methods TNN-RTPCA, two state-of-the-art methods including DECOLOR [52] and BRTF [29]. All the parameters are set as recommended in the paper.

According to the FCA results of grayscale video in Section III-A, the zero-frequency component contains almost all of the background information and the moving object lies in the nonzero-frequency components. Thus we always keep zero frequency component and set the frequency-weighted vector α as :

$$\alpha = [0, +\infty, +\infty, \dots, +\infty]^T \quad (29)$$

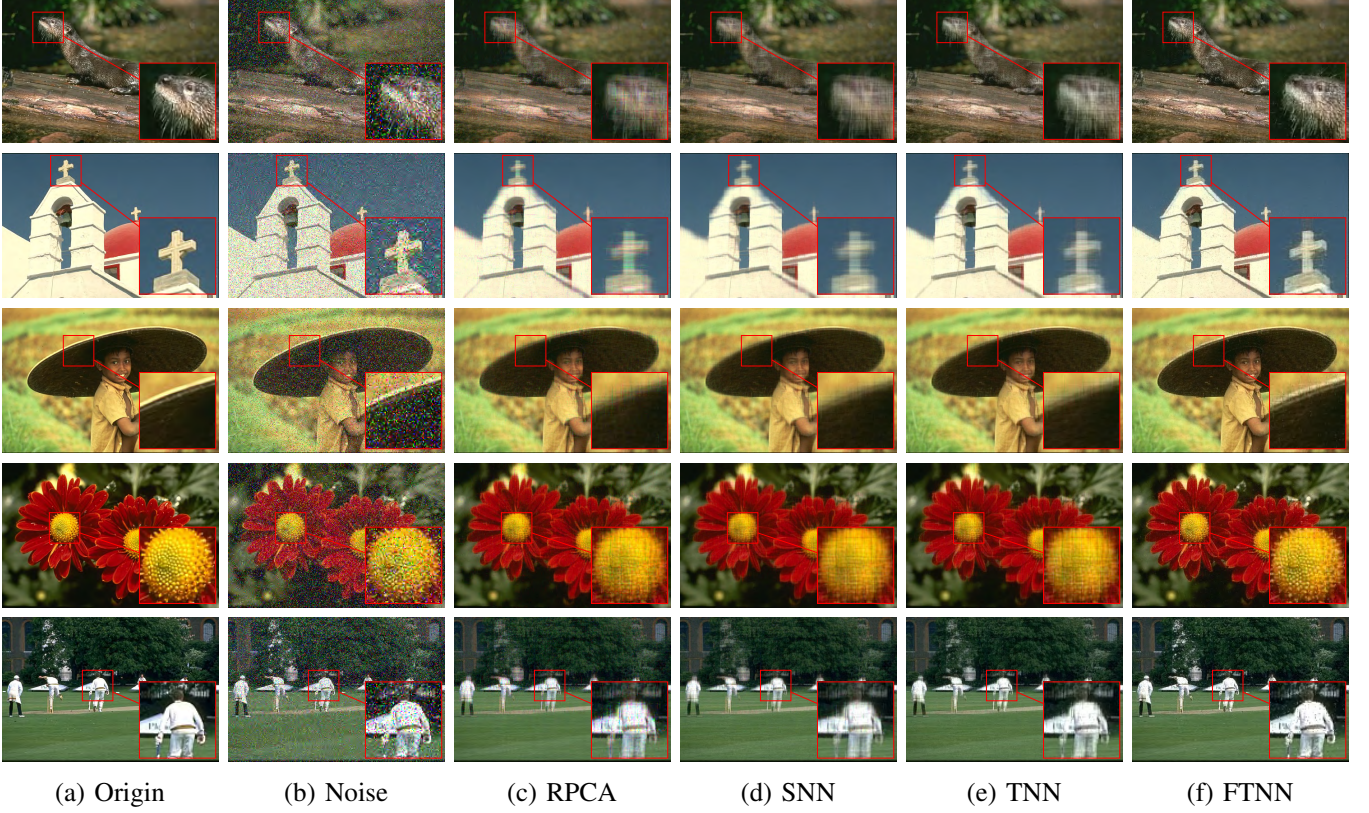


Fig. 13: Comparison of some examples on color image denoising with 20% noise. (a) Original images; (b) Noisy images; (c), (d), (e) and (f) are the recovery images by RPCA, SNN, TNN and FTNN respectively.

In this way, no SVDs are needed when calculating FTSVT operator to update the low-rank component. The computational cost will depend on the FFT in each iteration, which should make the proposed FTNN algorithm run much faster than other RPCA-based methods. We will discuss the comparison of running time later.

Six widely used metrics are used to evaluate the quality of the recovered background from video sequences as follows:

- 1) AGE (Average Gray-level Error), is the average of the gray-level absolute difference between ground-truth and the recovered background. Range in $[0, 255]$.
- 2) pEPs (Percentage of Error Pixels), is the percentage of error pixels, whose absolute difference between ground-truth and the recovered background is greater than a threshold, with respect to the total number of pixels in the image. Range in $[0, 1]$.
- 3) pCEPs (Percentage of Clustered Error Pixels), is the percentage of clustered error pixels, whose 4-connected neighbours are also error pixels, with respect to the total number of pixels in the image. Range in $[0, 1]$.
- 4) MSSSIM (Multi-Scale Structural Similarity Index), is the estimate of the perceived visual distortion. Range in $[-1, 1]$. Defined in [53], [54].
- 5) PSNR: Mentioned before in (26).
- 6) CQM (Color image Quality Measure), is a metric which is calculated in YUV color space and based on the PSNR computed in the single YUV band. Defined in [55].

For the first three evaluation metrics AGE, pEPs and pCEPs, the lower these values, the better the recovery background. For the last three evaluation metrics MSSSIM, PSNR and CQM, the higher these values, the better the recovered background.

Table III shows the evaluation metric results of different methods on five color video sequences. It can be seen that FTNN method can achieve the best precision of at least two metrics for all sequences. Meanwhile, compared with

TABLE III: Comparison of different evaluation metrics on background modeling

Sequence	Methods	AGE	pEPs	pCEPs	MSSSIM	PSNR	CQM
CAVIAR1	FTNN	3.0717	0.0037	0.0027	0.9917	33.6179	33.8376
	BRTF	3.7218	0.0052	0.0033	0.9793	32.6354	32.9582
	DECOLOR	3.2065	0.0030	0.0020	0.9896	32.4944	32.7749
	TNN	6.2369	0.0491	0.0410	0.8883	26.0245	26.6583
	RPCA	4.9186	0.0305	0.0253	0.9330	29.7088	30.1066
HumanBody2	FTNN	3.3397	0.0038	0.0003	0.9975	34.5978	35.0202
	BRTF	5.8037	0.0438	0.0262	0.9725	26.9631	27.5809
	DECOLOR	3.9077	0.0064	0.0006	0.9931	31.1452	31.0911
	TNN	5.0021	0.0208	0.0090	0.9890	30.6921	31.0409
	RPCA	5.1913	0.0252	0.0127	0.9866	29.8480	30.4087
HighwayI	FTNN	1.7890	0.0027	0.0004	0.9901	38.2507	39.1607
	BRTF	2.4575	0.0027	0.0004	0.9881	36.9758	37.8537
	DECOLOR	3.8674	0.0288	0.0175	0.9501	28.3436	29.2440
	TNN	4.4316	0.0056	0.0006	0.9401	32.2916	33.3336
	RPCA	2.7039	0.0049	0.0013	0.9826	36.3446	37.1835
HighwayII	FTNN	2.6195	0.0047	0.0000	0.9934	34.6171	35.4127
	BRTF	2.4876	0.0049	0.0000	0.9946	34.3662	35.0447
	DECOLOR	2.5498	0.0051	0.0001	0.9933	34.9028	35.6343
	TNN	3.3198	0.0058	0.0000	0.9881	32.3148	33.1945
	RPCA	2.4542	0.0055	0.0000	0.9938	33.5809	34.4022
IBMTest2	FTNN	2.7945	0.0006	0.0000	0.9957	36.6157	36.4704
	BRTF	4.3095	0.0048	0.0048	0.9945	33.5641	33.4791
	DECOLOR	4.2134	0.0031	0.0000	0.9941	34.1732	34.2890
	TNN	4.7225	0.0248	0.0130	0.9857	30.9800	31.3569
	RPCA	4.2342	0.0049	0.0006	0.9929	33.1650	33.3380

TABLE IV: Comparison of running time (seconds) on background modeling

Sequence	RPCA	TNN	DECOLOR	BRTF	FTNN
CAVIAR1	159.17	333.47	1266.84	210.24	43.05
HumanBody2	97.26	156.77	626.30	96.14	23.26
HighwayI	89.95	146.86	462.12	88.06	20.37
HighwayII	97.76	148.54	347.20	96.39	20.72
IBMTest2	103.63	151.55	281.21	97.59	18.19

RPCA and TNN, the results by BRTF, DECOLOR and FTNN methods have higher accuracy. Fig. 14 illustrates the recovered background image by five methods on CAVIAR1, HumanBody2, HighwayI, HighwayII and IBMTest2 sequences.

We can see that the background images recovered by TNN always have the foreground ghosting. It indicates that TNN can not remove the sparse foreground component sufficiently. BRTF method removes the foreground

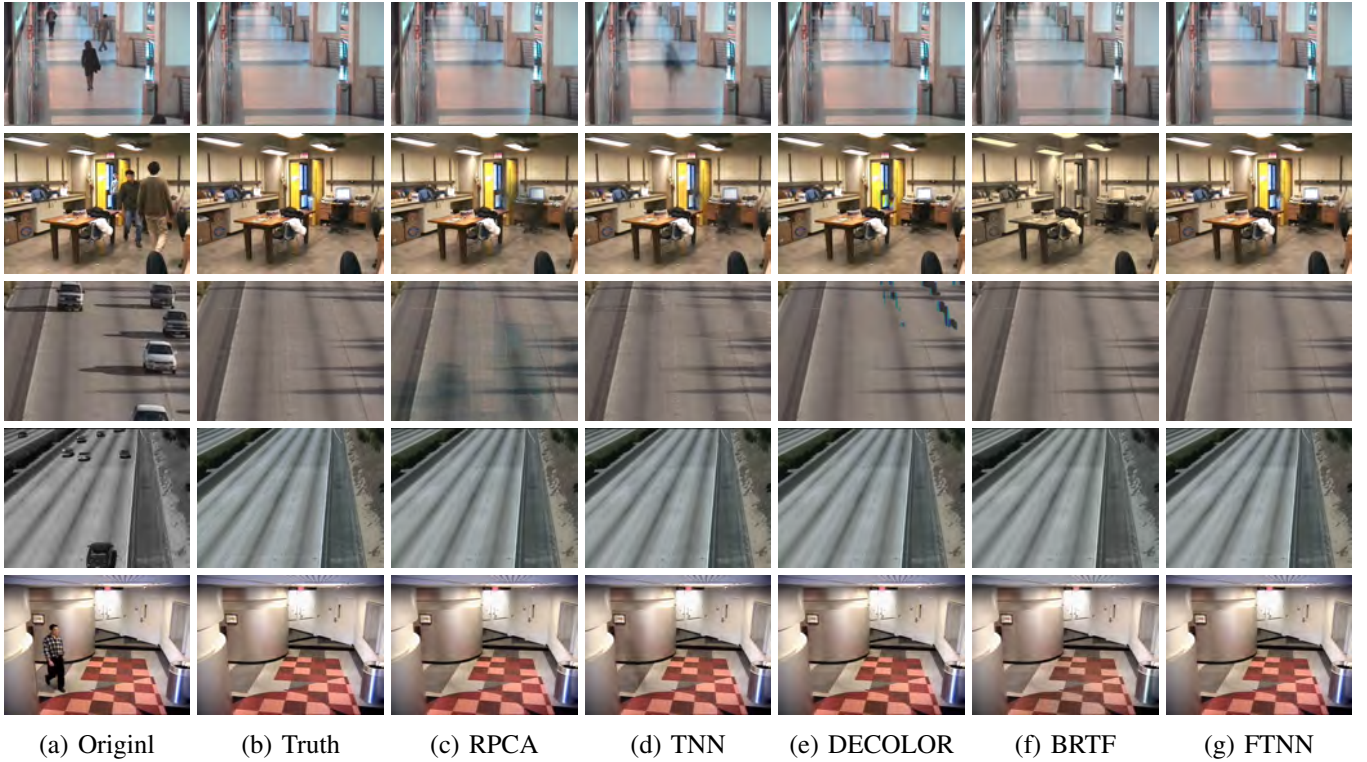


Fig. 14: Background modeling on different video sequences. From top to bottom are CAVIAR1, HumanBody2, HighwayI, HighwayII, IBMtest2 video sequences respectively.

very well but it has a distinct color distortion. DECOLOR can get a good background in most cases but performs badly in HighwayI sequence. As for our FTNN method, foreground pixels can be always removed sufficiently in all sequences and background information can be preserved very well.

Finally, Table IV shows the comparison of running time for all methods. It can be seen that the running time of the FTNN method is far less than the other methods, which verify the efficiency of our method. The reason is that we set the frequency-weighted vector to make our FTNN SVD-free as the computational costs of SVD are very expensive in RPCA-related problems.

Overall, according to the prior information of different data in the Fourier domain, the proposed method can adaptively choose the frequency-weighted vector and achieve better performance in accuracy and running time.

V. CONCLUSION

In this paper, we propose a novel robust tensor principal component analysis (RTPCA) method based on the frequency-weighted tensor nuclear norm (FTNN), which can make better use of the prior information in the frequency domain. We first give the frequency component analysis for some visual data. To implement Fourier filtering in the frequency domain, we then assign a frequency-weighting vector to frequency bands. Secondly, we define FTNN with respect to the weighting vector and rigorously deduce the frequency-weighted tensor singular value thresholding (FTSVT) operator which is related to solve low-rank component approximation problem. Experiments on synthetic 3D data discuss how to choose a appropriate weighting vector and show the superiority and flexibility of the proposed FTNN. Experiments on color image denoising and background modeling from video sequence shows the proposed method outperforms the existing methods in accuracy and running time.

REFERENCES

- [1] S. Wold, K. Esbensen, and P. Geladi, "Principal component analysis," *Chemometrics and intelligent laboratory systems*, vol. 2, no. 1-3, pp. 37–52, 1987.
- [2] M. A. Fischler and R. C. Bolles, "Random sample consensus: a paradigm for model fitting with applications to image analysis and automated cartography," *Communications of the ACM*, vol. 24, no. 6, pp. 381–395, 1981.

- [3] P. J. Huber and E. M. Ronchetti, "Robust statistics john wiley & sons," *New York*, vol. 1, no. 1, 1981.
- [4] F. De La Torre and M. J. Black, "A framework for robust subspace learning," *International Journal of Computer Vision*, vol. 54, no. 1-3, pp. 117–142, 2003.
- [5] R. Gnanadesikan and J. R. Kettenring, "Robust estimates, residuals, and outlier detection with multiresponse data," *Biometrics*, pp. 81–124, 1972.
- [6] Q. Ke and T. Kanade, "Robust l1 norm factorization in the presence of outliers and missing data by alternative convex programming," in *2005 IEEE Computer Society Conference on Computer Vision and Pattern Recognition (CVPR'05)*, vol. 1. IEEE, 2005, pp. 739–746.
- [7] E. J. Candès, X. Li, Y. Ma, and J. Wright, "Robust principal component analysis?" *Journal of the ACM (JACM)*, vol. 58, no. 3, pp. 1–37, 2011.
- [8] A. S. Georgiades, P. N. Belhumeur, and D. J. Kriegman, "From few to many: Illumination cone models for face recognition under variable lighting and pose," *IEEE Transactions on Pattern Analysis and Machine Intelligence*, vol. 23, no. 6, pp. 643–660, 2001.
- [9] B. k. Bao, G. Liu, C. Xu, and S. Yan, "Inductive robust principal component analysis," *IEEE Transactions on Image Processing*, vol. 21, no. 8, pp. 3794–3800, 2012.
- [10] Z. Wang and X. Xie, "An efficient face recognition algorithm based on robust principal component analysis," in *Proceedings of the Second International Conference on Internet Multimedia Computing and Service*. ACM, 2010, pp. 99–102.
- [11] J. Wright, A. Ganesh, S. Rao, Y. Peng, and Y. Ma, "Robust principal component analysis: Exact recovery of corrupted low-rank matrices via convex optimization," in *Advances in neural information processing systems*, 2009, pp. 2080–2088.
- [12] L. Li, W. Huang, I. Gu, and Q. Tian, "Statistical modeling of complex backgrounds for foreground object detection," *IEEE Transactions on Image Processing*, vol. 13, no. 11, pp. 1459–1472, 2004.
- [13] X. Cao, L. Yang, and X. Guo, "Total variation regularized rpca for irregularly moving object detection under dynamic background," *IEEE transactions on cybernetics*, vol. 46, no. 4, pp. 1014–1027, 2015.
- [14] S. Gu, Q. Xie, D. Meng, W. Zuo, X. Feng, and L. Zhang, "Weighted nuclear norm minimization and its applications to low level vision," *International journal of computer vision*, vol. 121, no. 2, pp. 183–208, 2017.
- [15] Q. Zhao, D. Meng, Z. Xu, W. Zuo, and L. Zhang, "Robust principal component analysis with complex noise," in *International conference on machine learning*, 2014, pp. 55–63.
- [16] Z. Lin, M. Chen, and Y. Ma, "The augmented lagrange multiplier method for exact recovery of corrupted low-rank matrices," *arXiv preprint arXiv:1009.5055*, 2010.
- [17] T. G. Kolda and B. W. Bader, "Tensor decompositions and applications," *SIAM Review*, vol. 66, no. 4, pp. 294–310, 2005.
- [18] A. Cichocki, D. Mandic, L. De Lathauwer, G. Zhou, Q. Zhao, C. Caiafa, and H. Phan, "Tensor decompositions for signal processing applications: From two-way to multiway component analysis," *IEEE Signal Processing Magazine*, vol. 32, no. 2, pp. 145–163, 2014.
- [19] H. Lu, K. Plataniotis, and A. N. Venetsanopoulos, "MPCA: Multilinear principal component analysis of tensor objects," *IEEE transactions on Neural Networks*, vol. 19, no. 1, pp. 18–39, 2008.
- [20] C. Lu, J. Feng, Y. Chen, W. Liu, Z. Lin, and S. Yan, "Tensor robust principal component analysis: Exact recovery of corrupted low-rank tensors via convex optimization," in *Proceedings of the IEEE conference on computer vision and pattern recognition*, 2016, pp. 5249–5257.
- [21] W. Cao, Y. Wang, J. Sun, D. Meng, C. Yang, A. Cichocki, and Z. Xu, "Total variation regularized tensor rpca for background subtraction from compressive measurements," *IEEE Transactions on Image Processing*, vol. 25, no. 9, pp. 4075–4090, 2016.
- [22] V. Lebedev, Y. Ganin, M. Rakhuba, I. Oseledets, and V. Lempitsky, "Speeding-up convolutional neural networks using fine-tuned cp-decomposition," *arXiv preprint arXiv:1412.6553*, 2014.
- [23] Q. Luo, Z. Han, X. Chen, Y. Wang, D. Meng, D. Liang, and Y. Tang, "Tensor rpca by bayesian cp factorization with complex noise," in *Proceedings of the IEEE International Conference on Computer Vision*, 2017, pp. 5019–5028.
- [24] Y. Liu, Z. Long, H. Huang, and C. Zhu, "Low cp rank and Tucker rank tensor completion for estimating missing components in image data," *IEEE Transactions on Circuits and Systems for Video Technology*, 2019.
- [25] E. Acar, D. M. Dunlavy, T. G. Kolda, and M. Mørup, "Scalable tensor factorizations for incomplete data," *Chemometrics and Intelligent Laboratory Systems*, vol. 106, no. 1, pp. 41–56, 2011.
- [26] P. Jain and S. Oh, "Provable tensor factorization with missing data," in *Advances in Neural Information Processing Systems*, 2014, pp. 1431–1439.
- [27] V. De Silva and L. Lim, "Tensor rank and the ill-posedness of the best low-rank approximation problem," *SIAM Journal on Matrix Analysis and Applications*, vol. 30, no. 3, pp. 1084–1127, 2008.
- [28] P. Rai, Y. Wang, S. Guo, G. Chen, D. Dunson, and L. Carin, "Scalable bayesian low-rank decomposition of incomplete multiway tensors," in *International Conference on Machine Learning*, 2014, pp. 1800–1808.
- [29] Q. Zhao, G. Zhou, L. Zhang, A. Cichocki, and S. Amari, "Bayesian robust tensor factorization for incomplete multiway data," *IEEE transactions on neural networks and learning systems*, vol. 27, no. 4, pp. 736–748, 2015.
- [30] L. De Lathauwer, B. De Moor, and J. Vandewalle, "A multilinear singular value decomposition," *SIAM Journal on Matrix Analysis and Applications*, vol. 21, no. 4, pp. 1253–1278, 2000.
- [31] T. G. Kolda and B. Bader, "Tensor decompositions and applications," *SIAM review*, vol. 51, no. 3, pp. 455–500, 2009.
- [32] J. Liu, P. Musialski, P. Wonka, and J. Ye, "Tensor completion for estimating missing values in visual data," *IEEE transactions on pattern analysis and machine intelligence*, vol. 35, no. 1, pp. 208–220, 2012.
- [33] D. Goldfarb and Z. Qin, "Robust low-rank tensor recovery: Models and algorithms," *SIAM Journal on Matrix Analysis and Applications*, vol. 35, no. 1, pp. 225–253, 2014.
- [34] B. Huang, C. Mu, D. Goldfarb, and J. Wright, "Provable low-rank tensor recovery," *Optimization-Online*, vol. 4252, no. 2, 2014.
- [35] M. E. Kilmer and C. D. Martin, "Factorization strategies for third-order tensors," *Linear Algebra and its Applications*, vol. 435, no. 3, pp. 641–658, 2011.
- [36] K. Braman, "Third-order tensors as linear operators on a space of matrices," *Linear Algebra and Its Applications*, vol. 433, no. 7, pp. 1241–1253, 2010.

- [37] M. E. Kilmer, K. Braman, N. Hao, and R. C. Hoover, "Third-order tensors as operators on matrices: A theoretical and computational framework with applications in imaging," *SIAM Journal on Matrix Analysis and Applications*, vol. 34, no. 1, pp. 148–172, 2013.
- [38] Z. Zhang, G. Ely, S. Aeron, N. Hao, and M. Kilmer, "Novel methods for multilinear data completion and de-noising based on tensor-svd," *Computer Science*, vol. 44, no. 9, pp. 3842–3849, 2014.
- [39] C. Lu, J. Feng, W. Liu, Z. Lin, S. Yan *et al.*, "Tensor robust principal component analysis with a new tensor nuclear norm," *IEEE transactions on pattern analysis and machine intelligence*, 2019.
- [40] L. Chen, Y. Liu, and C. Zhu, "Iterative block tensor singular value thresholding for extraction of low rank component of image data," in *2017 IEEE International Conference on Acoustics, Speech and Signal Processing (ICASSP)*. IEEE, 2017, pp. 1862–1866.
- [41] L. Feng, Y. Liu, L. Chen, X. Zhang, and C. Zhu, "Robust block tensor principal component analysis," *Signal Processing*, vol. 166, p. 107271, 2020.
- [42] Y. Liu, L. Chen, and C. Zhu, "Improved robust tensor principal component analysis via low-rank core matrix," *IEEE Journal of Selected Topics in Signal Processing*, vol. 12, no. 6, pp. 1378–1389, 2018.
- [43] H. Kong, X. Xie, and Z. Lin, "t-schatten- p norm for low-rank tensor recovery," *IEEE Journal of Selected Topics in Signal Processing*, vol. 12, no. 6, pp. 1405–1419, 2018.
- [44] P. Zhou and J. Feng, "Outlier-robust tensor pca," in *Proceedings of the IEEE Conference on Computer Vision and Pattern Recognition*, 2017, pp. 2263–2271.
- [45] M. Baburaj and S. N. George, "Reweighted low-rank tensor decomposition based on t-svd and its applications in video denoising," *arXiv preprint arXiv:1611.05963*, 2016.
- [46] O. Rojo and H. Rojo, "Some results on symmetric circulant matrices and on symmetric centrosymmetric matrices," *Linear algebra and its applications*, vol. 392, pp. 211–233, 2004.
- [47] L. Maddalena and A. Petrosino, "Towards benchmarking scene background initialization," in *International conference on image analysis and processing*. Springer, 2015, pp. 469–476.
- [48] D. Martin, C. Fowlkes, D. Tal, J. Malik *et al.*, "A database of human segmented natural images and its application to evaluating segmentation algorithms and measuring ecological statistics." *Iccv Vancouver*., 2001.
- [49] J.-F. Cai, E. J. Candès, and Z. Shen, "A singular value thresholding algorithm for matrix completion," *SIAM Journal on optimization*, vol. 20, no. 4, pp. 1956–1982, 2010.
- [50] S. Boyd, N. Parikh, E. Chu, B. Peleato, J. Eckstein *et al.*, "Distributed optimization and statistical learning via the alternating direction method of multipliers," *Foundations and Trends® in Machine learning*, vol. 3, no. 1, pp. 1–122, 2011.
- [51] C. Lu, J. Tang, S. Yan, and Z. Lin, "Generalized nonconvex nonsmooth low-rank minimization," in *Proceedings of the IEEE conference on computer vision and pattern recognition*, 2014, pp. 4130–4137.
- [52] X. Zhou, C. Yang, and W. Yu, "Moving object detection by detecting contiguous outliers in the low-rank representation," *IEEE transactions on pattern analysis and machine intelligence*, vol. 35, no. 3, pp. 597–610, 2012.
- [53] Z. Wang, E. P. Simoncelli, and A. C. Bovik, "Multiscale structural similarity for image quality assessment," in *The Thrity-Seventh Asilomar Conference on Signals, Systems & Computers, 2003*, vol. 2. Ieee, 2003, pp. 1398–1402.
- [54] Z. Wang, A. Bovik, H. Sheikh, E. Simoncelli *et al.*, "Image quality assessment: from error visibility to structural similarity," *IEEE transactions on image processing*, vol. 13, no. 4, pp. 600–612, 2004.
- [55] Y. Yalman and I. ERTÜRK, "A new color image quality measure based on yuv transformation and psnr for human vision system," *Turkish Journal of Electrical Engineering & Computer Sciences*, vol. 21, no. 2, pp. 603–612, 2013.